

Pose2Room: Understanding 3D Scenes from Human Activities

Yinyu Nie¹ Angela Dai¹ Xiaoguang Han² Matthias Nießner¹
¹Technical University of Munich ²SRIBD, CUHKSZ

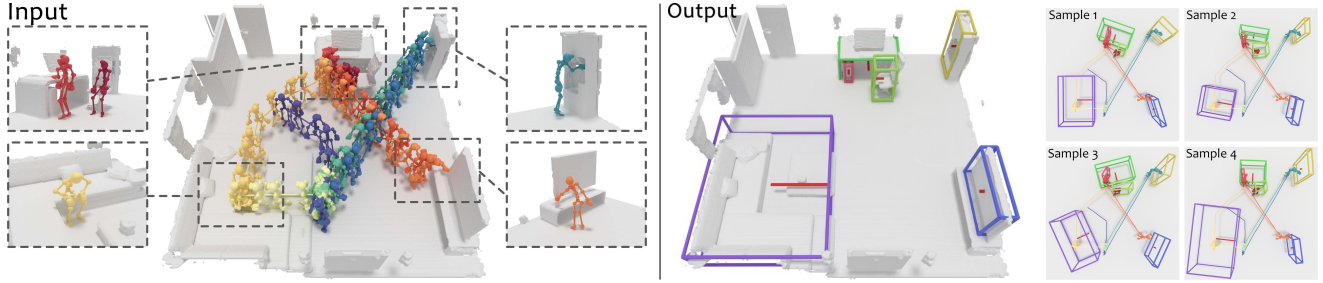


Figure 1. From an observed pose trajectory of a person performing daily activities in an indoor scene (left), we learn to estimate likely object configurations of the scene underlying these interactions, as set of object class labels and oriented 3D bounding boxes (middle). By sampling from our probabilistic decoder, we synthesize multiple plausible object arrangements (right). (Scene geometry is shown only for visualization.)

Abstract

With wearable IMU sensors, one can estimate human poses from wearable devices without requiring visual input [63]. In this work, we pose the question: Can we reason about object structure in real-world environments solely from human trajectory information? Crucially, we observe that human motion and interactions tend to give strong information about the objects in a scene – for instance a person sitting indicates the likely presence of a chair or sofa. To this end, we propose P2R-Net to learn a probabilistic 3D model of the objects in a scene characterized by their class categories and oriented 3D bounding boxes, based on an input observed human trajectory in the environment. P2R-Net models the probability distribution of object class as well as a deep Gaussian mixture model for object boxes, enabling sampling of multiple, diverse, likely modes of object configurations from an observed human trajectory. In our experiments we demonstrate that P2R-Net can effectively learn multi-modal distributions of likely objects for human motions, and produce a variety of plausible object structures of the environment, even without any visual information.

1. Introduction

Understanding the structure of real-world 3D environments is fundamental to many computer vision tasks, and there has been a well-studied history of research into 3D reconstruction from various visual input mediums, such as

RGB video [14, 44, 54, 56], RGB-D video [7, 10, 46, 49, 67], or single images [9, 15, 28, 36, 37, 47, 51, 72]. Such approaches have shown impressive capture of geometric structures leveraging strong visual signals. We consider an unconventional view of 3D perception: in the case of a lack of any visual signal, we look at human pose data, which for instance can be estimated from wearable IMU sensors [20, 29, 63], and ask “What can we learn about a 3D environment from only human pose trajectory information?”

In particular, we observe that human movement in a 3D environment often interacts both passively and actively with objects in the environment, giving strong cues about likely objects and their locations. For instance, walking around a room indicates where empty floor space is available, a sitting motion indicates high likelihood of a chair or sofa to support the sitting pose, and a single outstretched arm suggests picking up/putting down an object to furniture that supports the object. We thus propose to address a new scene estimation task: from only a sequence observation of 3D human poses, to estimate the object arrangement in the scene of the objects the person has interacted with, as a set of object class categories and 3D oriented bounding boxes.

As there are inherent ambiguities that lie in 3D object localization from only a human pose trajectory in the scene, we propose P2R-Net to learn a probabilistic model of the most likely modes of object configurations in the scene. From the sequence of poses, P2R-Net leverages the pose joint locations to vote for potential object centers that participate in the observed pose interactions. We then intro-

duce a probabilistic decoder that learns a Gaussian mixture model for object box parameters, from which we can sample multiple diverse hypotheses of object arrangements.

In summary, we present the following contributions:

- We propose a new perspective on 3D scene understanding by studying estimation of 3D object configurations from solely observing 3D human pose sequences of interactions in an environment, without any visual input, and predicting the object class categories and 3D oriented bounding boxes of the interacted objects in the scene.
- To address this task, we introduce a new, end-to-end, learned probabilistic model that estimates probability distributions for the object class categories and bounding box parameters.
- We demonstrate that our model captures complex, multi-modal distributions of likely object configurations, which can be sampled to produce diverse hypotheses that have accurate coverage over the ground truth object arrangement.

2. Related Work

Predicting Human Interactions in Scenes. Capturing and modeling interactions between human and scenes has seen impressive progress in recent years, following significant advances in 3D reconstruction and 3D deep learning. From a visual observation of a scene, interactions and human-object relations are estimated. Several methods have been proposed for understanding the relations between scene and human poses via object functionality prediction [21,27,50,75] and affordance analysis [13,22,55,58,59,65].

By parsing the physics and semantics in human interactions, further works have been proposed towards synthesizing static human poses or human body models into 3D scenes [21,22,25,26,35,57,58,73,74]. These works focus on how to place human avatars into a 3D scene with semantic and physical plausibility (e.g., support or occlusion constraints). Various approaches have additionally explored synthesizing dynamic motions for a given scene geometry. Early methods retrieve and integrate existing avatar motions from database to make them compatible with scene geometry [4,33,38,39,61]. Given a goal pose or a task, more recent works leverage deep learning methods to search for a possible motion path and estimate plausible contact motions [6,8,24,42,62,64]. These methods all explore human-scene interaction understanding by estimating object functionalities or human interactions as poses in a given 3D scene environment. In contrast, we take a converse perspective, and aim to estimate the 3D scene arrangement from human pose trajectory observations.

Scene Understanding with Human Priors. As many environments, particularly indoor scenes, have been designed for people’s daily usage, human behavioral priors can be leveraged to additionally reason about 2D or 3D scene observations. Various methods have been proposed to leverage human context as extra signal towards holistic perception to improve performance in scene understanding tasks such as semantic segmentation [11], layout detection from images [17,60], 3D object labeling [30], 3D object detection and segmentation [66], and 3D reconstruction [18,19].

Additionally, several methods learn joint distributions of human interactions with 3D scenes or RGB video that can be leveraged to re-synthesize the observed scene as an arranged set of synthetic, labeled CAD models [16,31,32,43,58]. Recently, HPS (Human POSEitioning System) [23] introduced an approach to simultaneously estimate human pose trajectory and 3D scene reconstruction from a set of wearable visual and inertial sensors on a person. We also aim to understand 3D scenes as arrangements of objects, but do not require any labeled interactions nor consider any visual (RGB, RGB-D, etc.) information as input. The recent approach of Mura et al. [45] poses the task of floor plan estimation from 2D human walk trajectories, and propose an approach to predict occupancy-based floor plans that indicate structure and object footprints, but without object instance distinction and employs a fully-deterministic prediction. To the best of our knowledge, we introduce the first method to learn 3D object arrangement distributions from only 3D human pose trajectories, without any visual input.

Pose Tracking with IMUs. Our method takes the input of human pose trajectories, which is built on the success of motion tracking techniques. Seminal work on pose estimation from wearable sensors have demonstrated effective pose estimation from wearable sensors, such as optical markers [5,24] or IMUs [20,29,34,40,63]. Our work is motivated by the capability of reliably estimating human pose from these simple sensor setups without any visual data, from which we aim to learn about human-object interaction priors to estimate scene object configurations.

3. Method

From only a human pose trajectory as input, we aim to estimate a distribution of likely object configurations, from which we can sample plausible hypotheses of objects in the scene as sets of class category labels and oriented 3D bounding boxes. We observe that most human interactions in an environment are targeted towards specific objects, and that general motion behavior is often influenced by the object arrangement in the scene. We thus aim to discover potential objects that each pose may be interacting with.

We first extract meaningful features from the human pose sequence with a *position encoder* to disentangle each

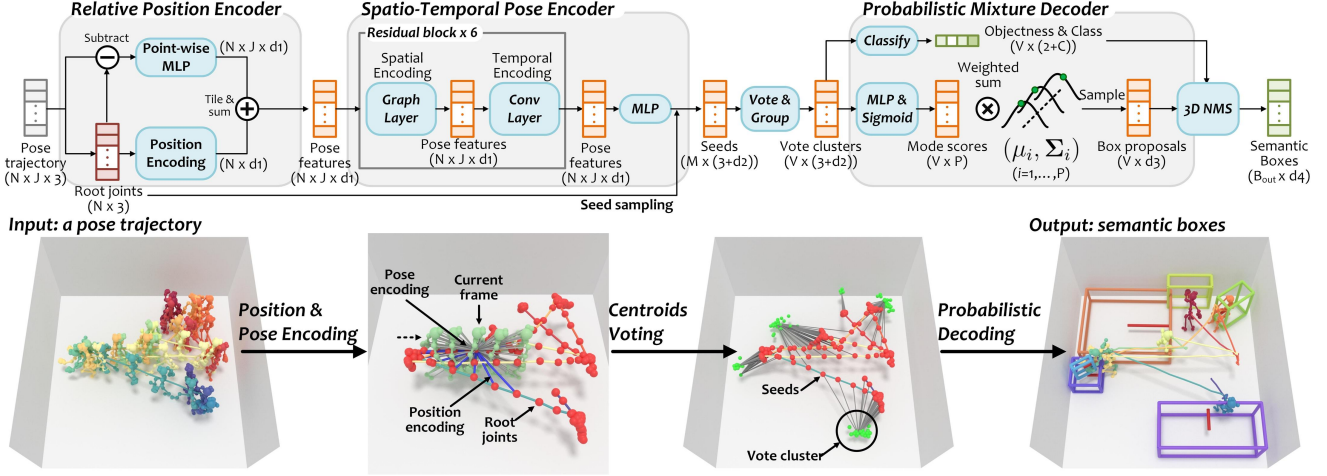


Figure 2. Overview of P2R-Net. Given a pose trajectory with N frames and J joints, a position encoder decouples each skeleton frame into a relative position encoding (from its root joint as the hip centroid) and a position-agnostic pose. After combining them, a pose encoder learns local pose features from both body joints per skeleton (spatial encoding) and their changes in consecutive frames (temporal encoding). Root joints as seeds are then used to vote for the center of a nearby object that each pose is potentially interacting with. A probabilistic mixture network learns likely object box distributions, from which object class labels and oriented 3D boxes can be sampled.

frame into a relative position encoding and a position-agnostic pose, as well as a *pose encoder* to learn the local spatio-temporal feature for each pose in consecutive frames. We then leverage these features to vote for a potential interacting object for each pose. From these votes, we learn a *probabilistic mixture decoder* to propose box proposals for each object, characterizing likely modes for objectness, class label, and box parameters. An illustration of our approach is shown in Figure 2.

3.1. Relative Position Encoding

We consider an input pose trajectory with N frames and J joints as the sequence of 3D locations $\mathbf{T} \in \mathbb{R}^{N \times J \times 3}$. We also denote the root joint of each pose by $\mathbf{r} \in \mathbb{R}^{N \times 3}$, where the root joint of a pose is the centroid of the joints corresponding to the body hip (for the full skeleton configuration, we refer to the supplemental). To learn informative pose features, we first disentangle for each frame the absolute pose joint coordinates into a relative position encoding $\mathbf{Q} \in \mathbb{R}^{N \times d_1}$ and a position-agnostic pose feature $\mathbf{P} \in \mathbb{R}^{N \times J \times d_1}$, which are formulated as follows:

$$\begin{aligned} \mathbf{Q} &= \text{Pool}[f_1(\mathcal{N}(\mathbf{r}) - \mathbf{r})], \\ \mathbf{P} &= f_2(\mathbf{T} - \mathbf{r}), \quad \mathcal{N}(\mathbf{r}) \in \mathbb{R}^{N \times k \times 3}, \end{aligned} \quad (1)$$

where $f_1(\cdot)$, $f_2(\cdot)$ are point-wise MLP layers. $\mathcal{N}(\mathbf{r})$ is the set of k temporal neighbors to each root joint in \mathbf{r} , and $\text{Pool}(\cdot)$ denotes neighbor-wise average pooling. By broadcast summation, we output $\mathbf{P}^r = \mathbf{P} + \mathbf{Q}$ for further spatio-temporal pose encoding. Understanding relative positions rather than absolute positions helps to provide more generalizable features to understand common pose motion in var-

ious object interactions, as these human-object interactions typically occur locally in a scene.

3.2. Spatio-Temporal Pose Encoding

The encoding \mathbf{P}^r provides signal for the relative pose trajectory of a person. We then further encode these features to capture the joint movement to understand local human-object interactions. That is, from \mathbf{P}^r , we learn joint movement in spatio-temporal domain: (1) in the spatial domain, we learn from intra-skeleton joints to capture per-frame pose features; (2) in the temporal domain, we learn from inter-frame relations to perceive each joint's movement.

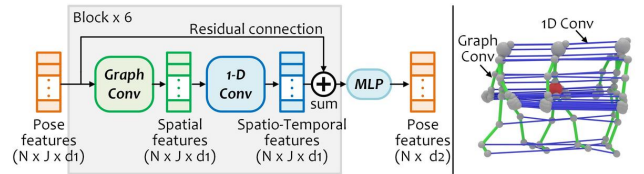


Figure 3. Pose encoding with spatio-temporal convolutions.

Inspired by [70] in 2D pose recognition, we first use a graph convolution layer to learn intra-skeleton joint features. Edges in the graph convolution are constructed following the skeleton bones, which encodes skeleton-wise spatial information. For each joint, we then use a 1-D convolution layer to capture temporal features from its inter-frame neighbors. A graph layer and an 1-D convolution layer are linked into a block with a residual connection to process the input \mathbf{P}^r (see Figure 3). By stacking six blocks, we obtain a deeper spatio-temporal pose encoder with a wider receptive field in temporal domain, enabling reason-

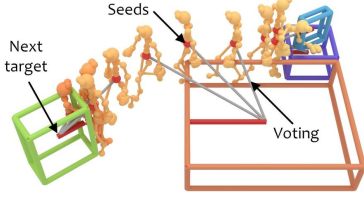


Figure 4. Voting to objects that potentially influence the motion trajectory in approaching the target.

ing over more temporal neighbors for object box estimation. Finally, we adopt an MLP to process all joints per skeleton to obtain pose features $\mathbf{P}^{st} \in \mathbb{R}^{N \times d_2}$.

3.3. Locality-Sensitive Voting

With our extracted pose features \mathbf{P}^{st} , we then learn to vote for all the objects a person could have interacted with in a trajectory (see Figure 2). For each pose frame, we predict the center of an object it potentially interacts with. Since we do not know when interactions begin or end, each pose votes for a potential object interaction. As human motion in a scene will tend to active interaction with an object or movement to an object, we aim to learn these patterns by encouraging votes for objects close to the respective pose, encouraging locality-based consideration.

For each pose feature $p^{st} \in \mathbf{P}^{st}$, we use its root joint $r \in \mathbf{r}$ as a seed location, and vote for an object center by learning the displacement from the seed:

$$\begin{aligned} \mathbf{v} &= \mathbf{r}_s + f_3(\mathbf{P}_s^{st}), \quad \mathbf{r}_s, \mathbf{v} \in \mathbb{R}^{M \times 3}, \\ \mathbf{P}^v &= \mathbf{P}_s^{st} + f_4(\mathbf{P}_s^{st}), \quad \mathbf{P}_s^{st}, \mathbf{P}^v \in \mathbb{R}^{M \times d_2}, \end{aligned} \quad (2)$$

where \mathbf{r}_s are the uniformly sampled M seeds from \mathbf{r} to ensure a even spatial distribution; \mathbf{P}_s^{st} are the corresponding pose features of \mathbf{r}_s ; f_3, f_4 are MLP layers; \mathbf{v}, \mathbf{P}^v denote the vote coordinates and features learned from \mathbf{P}_s^{st} .

Since there are several objects in a scene, for each seed, we vote for the center to the nearest one (see Figure 4). The nearest object is both likely to participate in a nearby interaction, and affect motion around the object if not directly participating in an interaction. This strategy helps to reduce the ambiguities in the task of scene object configuration estimation from a pose trajectory by capturing both direct and indirect effects of object location on pose movement.

For the seeds which vote for the same object, we group their votes to a cluster following [53]. This outputs cluster centers $\mathbf{v}^c \in \mathbb{R}^{V \times 3}$ with aggregated cluster feature $\mathbf{P}^c \in \mathbb{R}^{V \times d_2}$ where V denotes the number of vote clusters. We then use the \mathbf{P}^c to decode to distributions that characterize semantic 3D boxes, which is described in Section 3.4. For poses whose root joint is not close to any object during training (beyond a distance threshold t_d), we consider them to have little connection with the objects, and do not train them to vote for any object.

3.4. Probabilistic Mixture Decoder

We decode vote clusters $(\mathbf{v}^c, \mathbf{P}^c)$ to propose oriented 3D bounding boxes for each object, along with their class label and objectness score. Each box is represented by a 3D center c , 3D size s and 1D orientation θ , where we represent the size by $\log(s)$ and orientation by $(\sin(\theta), \cos(\theta))$ for regression, similar to [71]. Since the nature of our task is inherently ambiguous (e.g., it may be unclear from observing a person sit if they are sitting on a chair or a sofa, or the size of the sofa), we propose to learn a probabilistic mixture decoder to predict the box centroid, size and orientation with multiple modes, from a vote cluster $\mathbf{v}^c \in \mathbf{v}^c, \mathbf{P}^c \in \mathbf{P}^c$:

$$\begin{aligned} y_\tau &= \sum_{k=1}^P f_\tau^k(\mathbf{P}^c) \cdot y_\tau^k, \quad \tau \in \{c, s, \theta\}, \\ y_c^* &= \mathbf{v}^c + y_c, \quad y_\tau^k \sim \mathcal{N}(\mu_\tau^k, \Sigma_\tau^k), \quad y_\tau, y_\tau^k \in \mathbb{R}^{d_\tau}, \end{aligned} \quad (3)$$

where $\tau \in \{c, s, \theta\}$ denote the regression targets for center, size, and orientation; $\mathcal{N}(\mu_\tau^k, \Sigma_\tau^k)$ is the learned multi-variate Gaussian distribution of the k -th mode for τ , where y_τ^k is sampled from; P is the number of Gaussian distributions (i.e., modes); $f_\tau^k(*) \in [0, 1]$ is the learned score for the k -th mode; y_τ is the weighted sum of the samples from all modes, which is the prediction of the center/size/orientation; and d_τ is their output dimension ($d_c=3, d_s=3, d_\theta=2$). Note that the box center y_c^* is obtained by regressing the offset y_c from cluster center \mathbf{v}^c . We predict the proposal objectness and the probability distribution for class category directly from \mathbf{P}^c , using an MLP.

Multi-modal Prediction. In Eq. 3, the learnable parameters are $f_\tau(*)$ and (μ_τ, Σ_τ) . $f_\tau(*)$ is realized with an MLP followed by a sigmoid function, and (μ_τ, Σ_τ) are the learned embeddings shared among all samples. During training, we sample y_τ^k from each mode $\mathcal{N}(\mu_\tau^k, \Sigma_\tau^k)$ and predict y_τ using Eq. 3. To generate diverse and plausible hypotheses during inference, we not only sample y_τ^k , but also sample various different modes by randomly disregarding mixture elements based on their probabilities $f_\tau(*)$. Then we obtain y_τ as follows:

$$y_\tau = \sum_{k=1}^P I_\tau^k \cdot y_\tau^k, \quad I_\tau^k \sim \text{Bern}(f_\tau^k), \quad y_\tau^k \sim \mathcal{N}(\mu_\tau^k, \Sigma_\tau^k), \quad (4)$$

where I_τ^k is sampled from Bernoulli distribution with probability of $f_\tau^k(*)$. We also sample the object classes by the predicted classification probabilities, and discard proposed object boxes with low objectness ($\leq t_o$) after 3D NMS.

We can then generate N_h hypotheses in a scene; each hypothesis is an average of N_s samples of y_τ , which empirically strikes a good balance between diversity and accuracy of the set of hypotheses. To obtain the maximum likelihood prediction, we use $f_\tau^k(*)$ and the mean value μ_τ^k instead of I_τ^k and y_τ^k to estimate the boxes with Eq. 3.

3.5. Loss Function

The loss function consists of classification losses for objectness \mathcal{L}_{obj} and class label \mathcal{L}_{cls} , and regression losses for votes \mathcal{L}_v , box center \mathcal{L}_c , size \mathcal{L}_s and orientation angle \mathcal{L}_θ .

Classification Losses. Similar to [53], \mathcal{L}_{obj} and \mathcal{L}_{cls} are supervised by cross entropy losses, wherein the objectness score is used to classify if a vote cluster center is close to (≤ 0.3 m, positive) or far from (≥ 0.6 m, negative) the ground truth. Proposals from the clusters with positive objectness are further supervised with box regression losses.

Regression Losses. We supervise all the predicted votes, box centers, sizes and orientations with a Huber loss. For poses that are located within d_p to objects ($d_p = 1$ m), we use the closest object center to supervise their vote. Votes from those poses that are far from all objects are not considered. For center predictions, we use their nearest ground-truth center to calculate \mathcal{L}_c . Since box sizes and orientations are predicted from vote clusters, we use the counterpart from the ground-truth box that is nearest to the vote cluster for supervision. Then the final loss function is $\mathcal{L} = \sum_{\tau} \lambda_{\tau} \mathcal{L}_{\tau}$, where $\mathcal{L}_{\tau} \in \{\mathcal{L}_{obj}, \mathcal{L}_{cls}, \mathcal{L}_v, \mathcal{L}_c, \mathcal{L}_s, \mathcal{L}_\theta\}$ and $\{\lambda_{\tau}\}$ are constant weights that balance the losses.

4. Experiment Setup

Dataset. We introduce a new dataset for the task of estimating scene object configuration from a human pose trajectory observation, as existing interaction-based datasets are limited to single objects, focus on 2D data without 3D information, rely on imprecise pose tracking, or lack dynamics with only static interactions. We construct our dataset using the simulation environment VirtualHome [52], which is built on the Unity3D game engine. It consists of 29 rooms, with each room containing 88 objects on average; each object is annotated with available interaction types. VirtualHome allows customization of action scripts and control over humanoid agents to execute a series of complex interactive tasks. We refer readers to [52] for the details of the scene and action types. In our work, we focus on the static, interactable objects under 17 common class categories. In each room, we select up to 10 random objects to define the scene, and script the agent to interact with each of the objects in a sequential fashion. For each object, we also select a random interaction type associated with the object class category. Then we randomly sample 14K different sequences with corresponding object boxes to construct the dataset. During training, we also randomly flip, rotate and translate the scenes and poses for data augmentation. For additional detail about data generation, we refer to the supplemental.

Implementation. We train our P2R-Net end-to-end from scratch with the batch size at 32 on 4 NVIDIA 2080 Ti GPUs for 180 epochs until convergence, where Adam is used as the optimizer. The initial learning rate is at 1e-

3 in the first 80 epochs, which is decayed by $0.1 \times$ every 40 epochs after that. The losses are weighted by $\lambda_{obj}=5$, $\lambda_{cls}=1$, $\lambda_v=\lambda_c=\lambda_s=\lambda_\theta=10$ to balance the loss values. During training, we use pose distance threshold $t_d=1$ m. At inference time, we output box predictions after 3D NMS with an IoU threshold of 0.1. We use an objectness threshold of $t_o=0.5$. For more detailed architecture and data specifications, we refer to the supplemental.

Evaluation. To evaluate our task, we consider two types of evaluation splits: a sequence-level split \mathcal{S}_1 across different interaction sequences, and room-level split \mathcal{S}_2 across different rooms as well as interaction sequences. Note that sequences are trained with and evaluated against only the objects that are interacted with during the input observation, resulting in different variants of each room under different interaction sequences. For \mathcal{S}_1 , the train/test split ratio is 4:1 over the generated sequences. \mathcal{S}_2 is a more challenging setup, with 27 train rooms and 2 test rooms, resulting in 13K/1K sequences. Since the task is inherently ambiguous, and only a single ground truth configuration of each room is available, we evaluate multi-modal predictions by several metrics: *mAP@0.5* evaluates the mean average precision with the IoU threshold at 0.5 of the maximum likelihood prediction; *MMD* evaluates the Minimal Matching Distance [3] of the best matching prediction with the ground truth out of 10 sampled hypotheses to measure their quality; *TMD* evaluates the Total Mutual Diversity [69] to measure the diversity of the 10 hypotheses. We provide additional detail about MMD and TMD in the supplemental.

5. Results and Analysis

We evaluate our approach on the task of scene object configuration estimation from a pose trajectory observation, in comparison with baselines constructed from state-of-the-art 3D detection and pose understanding methods, as well as an ablation analysis of our multi-modal prediction.

5.1. Baselines

Since there are no prior works that tackle the task of predicting the object configuration of a scene from solely a 3D pose trajectory, we construct several baselines leveraging state-of-the-art techniques as well as various approaches to estimate multi-modal distributions. We consider the following baselines: **1) Pose-VoteNet** [53]. Since VoteNet is designed for detection from point clouds, we replace their PointNet++ encoder with our position encoder + MLPs to learn joint features for seeds. **2) Pose-VN**, Pose-VoteNet based on Vector Neurons [12] which replaces MLP layers in Pose-VoteNet with SO(3)-equivariant operators that can capture arbitrary rotations of poses to estimate objects. **3) Motion Attention** [41]. Since our task can be also regarded as a sequence-to-sequence problem, we adopt a frame-wise attention encoder to extract repetitive pose patterns in the

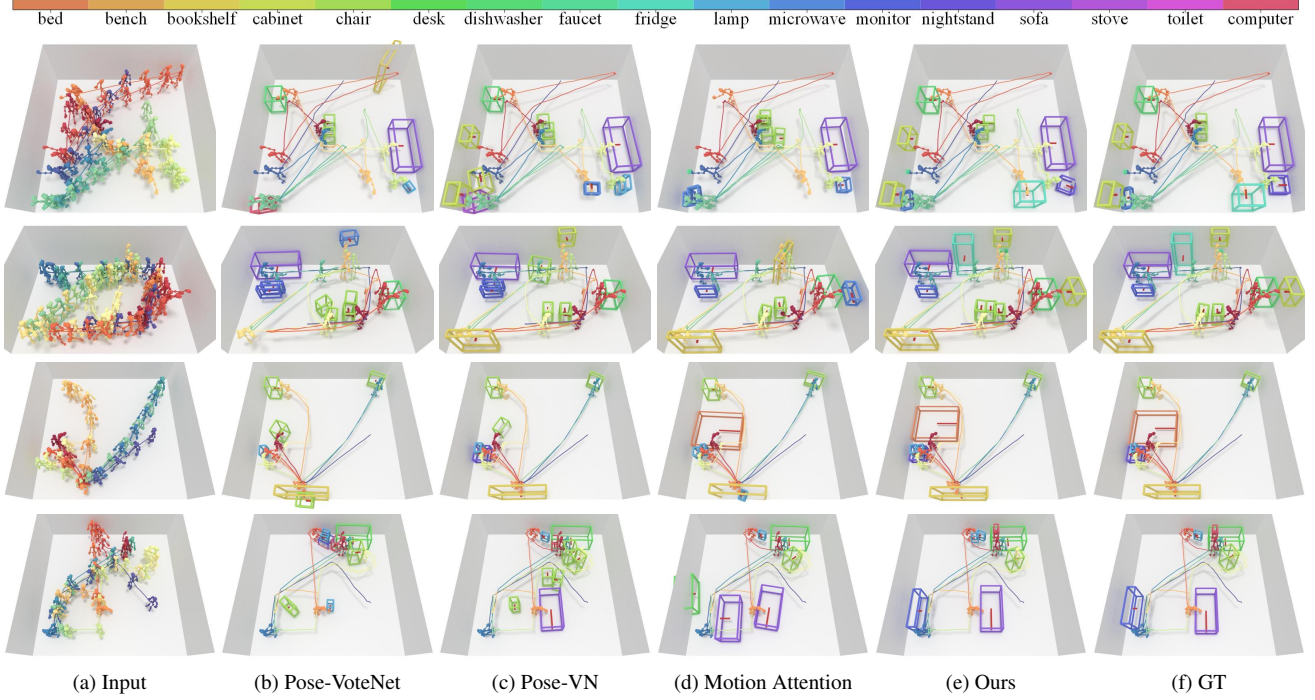


Figure 5. Qualitative results of object detection from a pose trajectory on the sequence-level split \mathcal{S}_1 (unseen interaction sequences).

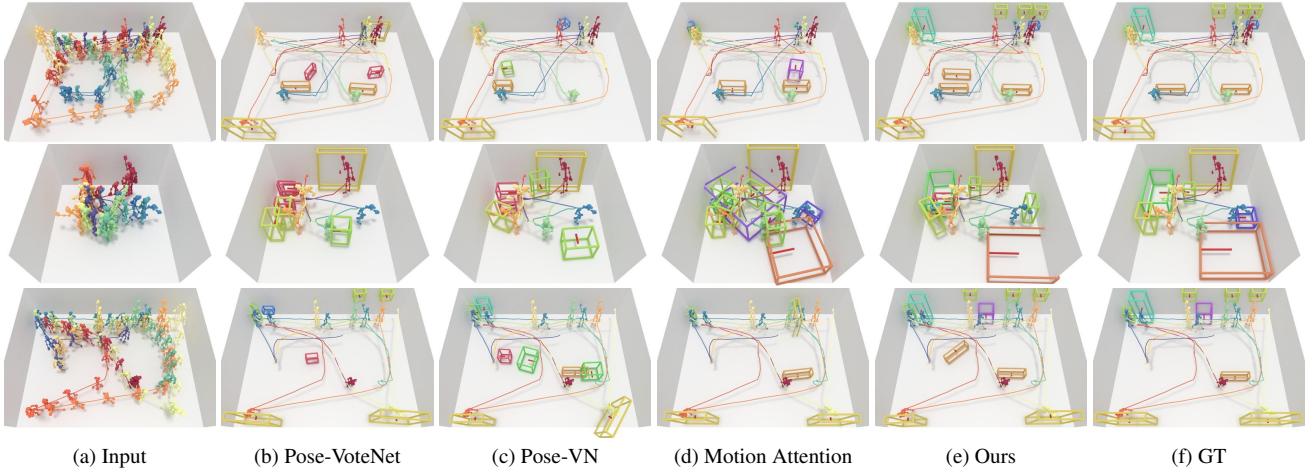


Figure 6. Qualitative results of object detection from a pose trajectory on the room-level split \mathcal{S}_2 (unseen interaction sequences and rooms).

temporal domain which then inform a VoteNet decoder to regress boxes. Additionally, we also ablate our probabilistic mixture decoder with other alternatives: **4) Deterministic P2R-Net (P2R-Net-D)**, where we use VoteNet decoder [53] in our method for box regression to produce deterministic results; **5) Generative P2R-Net (P2R-Net-G)**, where our P2R-Net decoder is designed with a probabilistic generative model [68] to decode boxes from a learned latent variable; **6) Heatmap P2R-Net (P2R-Net-H)**, where the box center, size and orientation are discretized into binary heatmaps, and the box regression is converted into a classification task. Detailed architecture specifications for these networks are

given in the supplemental material.

5.2. Qualitative Comparisons

Comparisons on \mathcal{S}_1 . Figure 5 visualizes predictions on the test set of unseen interaction sequences. Pose-VoteNet struggles to identify the existence of an object, leading to many missed detections, but can estimate reasonable object locations when an object is predicted. Pose-VN alleviates this problem of under-detection, but struggles to estimate object box sizes (rows 1,3). These baselines indicate the difficulty in detecting objects without sharing pose features among temporal neighbors. Motion Attention [41]

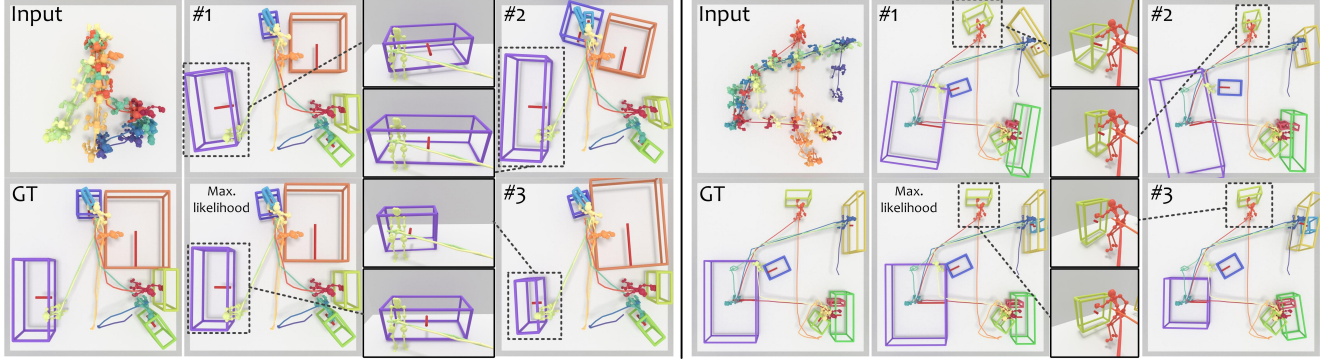


Figure 7. Multi-modal predictions of P2R-Net. By sampling our probabilistic decoder multiple times, we can obtain different plausible box predictions. Here, we show three randomly sampled hypotheses and the maximum likelihood prediction for each input.

	bed	bench	cabinet	chair	desk	dishwasher	fridge	lamp	sofa	stove	toilet	computer	mAP@0.5
Pose-VoteNet	2.90	15.00	33.14	18.77	58.52	32.14	0.00	6.07	62.32	49.82	0.00	3.06	25.70
Pose-VN	20.81	18.13	49.76	18.68	70.92	33.56	0.00	5.60	67.24	46.76	0.00	6.11	29.90
Motion Attention	36.42	7.54	23.35	19.50	77.71	15.59	17.13	2.35	78.61	51.03	14.81	5.50	28.39
P2R-Net-D	93.77	12.63	11.98	5.77	95.93	61.80	73.95	0.58	88.44	70.42	0.00	14.17	34.91
P2R-Net-G	91.69	7.56	36.61	10.05	93.47	67.53	77.45	1.21	92.97	64.86	5.56	18.67	37.48
P2R-Net-H	85.84	8.04	22.04	10.91	76.08	55.20	55.15	0.00	83.92	57.60	5.00	4.33	31.41
P2R-Net	94.21	10.12	54.72	8.02	93.32	56.33	59.89	3.25	90.92	57.86	61.11	19.94	42.20

Table 1. Quantitative evaluation on split \mathcal{S}_1 . For P2R-Net-G, P2R-Net-H and ours, we use the maximum likelihood predictions to calculate mAP scores. The mAP@0.5 is averaged over all 17 classes (see the full table with all classes in the supplementary file).

addresses this by involving global context with inter-frame attention. However, it does not take advantage of the skeleton’s spatial layout in continuous frames and struggles to detect the existence of objects (row 1,2). In contrast, our method leverages both target-dependent poses and object occupancy context, that learns the implicit interrelations between poses and objects to infer object boxes, and achieves better estimate of the scene configuration.

Comparisons on \mathcal{S}_2 . In Figure 6, we illustrate the qualitative comparisons on the test set of unseen interaction sequences in unknown rooms. In this scenario, most baselines fail to localize objects, while our method can nonetheless produce plausible object layouts.

Multi-modal Predictions. We additionally visualize various sampled hypotheses from our model \mathcal{S}_1 in Figure 7, showing that our method is able to deduce the spatial occupancy of objects from motion trajectories, and enables diverse, plausible estimation of object locations, orientation, and sizes for interactions.

5.3. Quantitative Comparisons

We use mAP@0.5 to measure object detection accuracy for all baselines, and evaluate the accuracy and diversity of a set of output hypotheses using minimal matching distance (MMD) and total mutual diversity (TMD).

Detection Accuracy. Table 1 shows a quantitative comparison on split \mathcal{S}_1 , where we observe that Pose-VoteNet and Pose-VN, struggle to recognize some object categories (e.g., bed, fridge and toilet). By leveraging the inter-frame

connections, Motion Attention achieves improved performance in recognizing object classes, but struggles with detecting objectness and predicting object sizes. In contrast, our position and pose encoder learns both the spatial and temporal signals from motions to estimate likely object locations by leveraging the potential connections between human and objects, with our probabilistic mixture decoder better capturing likely modalities in various challenging ambiguous interactions (e.g., toilet and cabinet). In Table 3, we compare mAP scores on split \mathcal{S}_2 , with increased relative improvement in the challenging scenario of scene object configuration estimation in new rooms.

	mAP@0.5	MMD	TMD
P2R-Net-G	37.48	37.43	1.73
P2R-Net-H	31.41	21.10	2.39
P2R-Net	42.20	38.28	3.34

Table 2. Comparisons on detection accuracy, and multi-modal quality and diversity on \mathcal{S}_1 . TMD=1 indicates no diversity.

Quality and Diversity of Multi-modal Predictions. We study the multi-modal predictions with our ablation variants P2R-Net-G and P2R-Net-H, and use MMD and TMD to evaluate the quality and diversity of 10 randomly sampled predictions for each method. From the 10 predictions, MMD records the best detection score (mAP@0.5), and TMD measures the average variance of the 10 semantic boxes per object. Table 2, 3 present the MMD and TMD scores on \mathcal{S}_1 and \mathcal{S}_2 respectively. P2R-Net-G tends to pre-

	mAP@0.5	MMD	TMD
Pose-VoteNet	10.23	-	-
Pose-VN	6.12	-	-
Motion Attention	6.53	-	-
P2R-Net-D	31.56	-	-
P2R-Net-G	31.59	31.83	1.98
P2R-Net-H	27.96	20.71	3.28
P2R-Net	35.34	32.47	4.35

Table 3. Comparisons on detection accuracy, and multi-modal quality and diversity on \mathcal{S}_2 . TMD=1 indicates no diversity.

dict with low diversity, as seen in low TMD score (TMD=1 indicates identical samples) and similar mAP@0.5 and MMD scores. P2R-Net-H shows better diversity but with lower accuracy in both of the two splits. Our final model not only achieves best detection accuracy, it also provides reasonable and diverse object configurations, with a notable performance improvement in the challenging \mathcal{S}_2 split.

5.4. Ablations

In Table 4, we explore the effects of each individual module (relative position encoder, spatio-temporal pose encoder and probabilistic mixture decoder). We ablate P2R-Net by gradually adding components from the baseline \mathbf{c}_0 : without relative position encoding (Pstn-Enc), where we use joints’ global coordinates relative to the room center; without spatio-temporal pose encoding (Pose-Enc), where we use MLPs to learn pose features from joint coordinates; without probabilistic mixture decoder (P-Dec), where we use 2-layer MLPs to regress box parameters.

$\mathcal{S}_1/\mathcal{S}_2$	Pstn-Enc	Pose-Enc	P-Dec	mAP@0.5
\mathbf{c}_0	-	-	-	8.71 / 3.12
\mathbf{c}_1	✓	-	-	34.43 / 19.07
\mathbf{c}_2	✓	✓	-	39.98 / 29.25
Full	✓	✓	✓	42.20 / 35.34

Table 4. Ablation study of our design choices.

From the comparisons, we observe that relative position encoding plays the most significant role. It allows our model to pick up on local pose signal, as many human-object interactions present with strong locality. The spatio-temporal pose encoder then enhances the pose feature learning, and enables our model to learn the joint changes both in spatial and temporal domains. This design largely improves our generalization ability, particularly in unseen rooms (from 19.07 to 29.25). The probabilistic decoder further alleviates the ambiguity of this problem, and combining all the modules together produces the best results.

Tolerance to noise. As real data often contain noise, we additionally study the effect of Gaussian noise (std=5 cm) onto the xyz coordinates of all joints in training and testing. Table 5 shows the effect of different noise levels in evaluation. We also visualize some sampled predictions under the

noise level at 10σ in Figure 8, where our method presents compelling tolerance for very noisy inputs.

Noise level	σ	2σ	3σ	5σ	10σ
\mathcal{S}_1	38.58	38.77	38.36	37.16	31.71
\mathcal{S}_2	27.16	26.13	27.72	29.18	26.18

Table 5. mAP@0.5 under varying levels of noise ($\sigma=1$ cm).

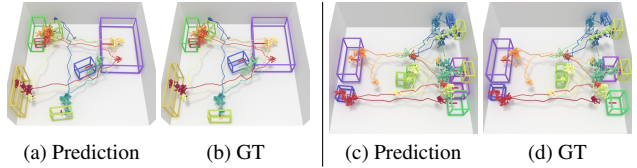


Figure 8. Predictions on noisy inputs (std=10 cm).

Limitations. Although P2R-Net achieves plausible scene estimations from only pose trajectories, it operates on several assumptions that can lead to potential limitations: (1) Objects should be interactable, e.g., our method may not detect objects that do not induce strong pose interactions like mirror or picture; (2) Interactions occur at close range, e.g., we may struggle to detect a TV from a person switching on it with a remote control. Additionally, we currently focus on estimating static object boxes. We believe an interesting avenue for future work is to characterize objects in motion (e.g., due to grabbing) or articulated objects (e.g., laptops).

Broader Impact. Our approach learns to infer scene configurations from human behavioral data, for which real-world data collection and use requires careful consideration to preserve privacy. Additionally, possible biases learned by our model could potentially be analyzed with uncertainty estimation techniques to discover model or data biases.

6. Conclusion

We have presented a first exploration to the ill-posed problem of estimating the 3D object configuration in a scene from only a 3D pose trajectory observation of a person interacting with the scene. Our proposed model P2R-Net leverages spatio-temporal features from the pose trajectory to vote for likely object positions and inform a new probabilistic mixture decoder that captures multi-modal distributions of object box parameters. We demonstrate that such a probabilistic approach can effectively model likely object configurations in scene, producing plausible object layout hypotheses from an input pose trajectory. We hope that this establishes a step towards object-based 3D understanding of environments using non-visual signal and opens up new possibilities in leveraging ego-centric motion for 3D perception and understanding.

Acknowledgements

This project is funded by the Bavarian State Ministry of Science and the Arts and coordinated by the Bavarian Research Institute for Digital Transformation (bidt), the TUM Institute of Advanced Studies (TUM-IAS), the ERC Starting Grant Scan2CAD (804724), and the German Research Foundation (DFG) Grant Making Machine Learning on Static and Dynamic 3D Data Practical.

References

- [1] Unity documentation: Humanbodybones. <https://docs.unity3d.com/ScriptReference/HumanBodyBones.html>, 03 2020. 12
- [2] Virtualhome homepage. <http://virtual-home.org/>, 11 2021. 14
- [3] Panos Achlioptas, Olga Diamanti, Ioannis Mitliagkas, and Leonidas Guibas. Learning representations and generative models for 3d point clouds. In *International conference on machine learning*, pages 40–49. PMLR, 2018. 5, 14
- [4] Shailen Agrawal and Michiel van de Panne. Task-based locomotion. *ACM Transactions on Graphics (TOG)*, 35(4):1–11, 2016. 2
- [5] Jinxiang Chai and Jessica K Hodgins. Performance animation from low-dimensional control signals. In *ACM SIGGRAPH 2005 Papers*, pages 686–696. 2005. 2
- [6] Yu-Wei Chao, Jimei Yang, Weifeng Chen, and Jia Deng. Learning to sit: Synthesizing human-chair interactions via hierarchical control. *arXiv preprint arXiv:1908.07423*, 2019. 2
- [7] Sungjoon Choi, Qian-Yi Zhou, and Vladlen Koltun. Robust reconstruction of indoor scenes. In *Proceedings of the IEEE Conference on Computer Vision and Pattern Recognition*, pages 5556–5565, 2015. 1
- [8] Enric Corona, Albert Pumarola, Guillem Alenya, and Francesc Moreno-Noguer. Context-aware human motion prediction. In *Proceedings of the IEEE/CVF Conference on Computer Vision and Pattern Recognition*, pages 6992–7001, 2020. 2
- [9] Manuel Dahnert, Ji Hou, , Matthias Nießner, and Angela Dai. Panoptic 3d scene reconstruction from a single rgb image. *Proc. Neural Information Processing Systems (NeurIPS)*, 2021. 1
- [10] Angela Dai, Matthias Nießner, Michael Zollhöfer, Shahram Izadi, and Christian Theobalt. Bundlefusion: Real-time globally consistent 3d reconstruction using on-the-fly surface reintegration. *ACM Transactions on Graphics (ToG)*, 36(4):1, 2017. 1
- [11] Vincent Delaitre, David F Fouhey, Ivan Laptev, Josef Sivic, Abhinav Gupta, and Alexei A Efros. Scene semantics from long-term observation of people. In *European conference on computer vision*, pages 284–298. Springer, 2012. 2
- [12] Congyue Deng, Or Litany, Yueqi Duan, Adrien Poulenard, Andrea Tagliasacchi, and Leonidas Guibas. Vector neurons: a general framework for so(3)-equivariant networks. *arXiv preprint arXiv:2104.12229*, 2021. 5, 13
- [13] Shengheng Deng, Xun Xu, Chaozheng Wu, Ke Chen, and Kui Jia. 3d affordancenet: A benchmark for visual object affordance understanding. In *Proceedings of the IEEE/CVF Conference on Computer Vision and Pattern Recognition*, pages 1778–1787, 2021. 2
- [14] Jakob Engel, Thomas Schöps, and Daniel Cremers. Lsdslam: Large-scale direct monocular slam. In *European conference on computer vision*, pages 834–849. Springer, 2014. 1
- [15] Francis Engelmann, Konstantinos Rematas, Bastian Leibe, and Vittorio Ferrari. From points to multi-object 3d reconstruction. In *Proceedings of the IEEE/CVF Conference on Computer Vision and Pattern Recognition*, pages 4588–4597, 2021. 1
- [16] Matthew Fisher, Manolis Savva, Yangyan Li, Pat Hanrahan, and Matthias Nießner. Activity-centric scene synthesis for functional 3d scene modeling. *ACM Transactions on Graphics (TOG)*, 34(6):1–13, 2015. 2
- [17] David F Fouhey, Vincent Delaitre, Abhinav Gupta, Alexei A Efros, Ivan Laptev, and Josef Sivic. People watching: Human actions as a cue for single view geometry. In *European Conference on Computer Vision*, pages 732–745. Springer, 2012. 2
- [18] Sam Fowler, Hansung Kim, and Adrian Hilton. Towards complete scene reconstruction from single-view depth and human motion. In *BMVC*, 2017. 2
- [19] Sam Fowler, Hansung Kim, and Adrian Hilton. Human-centric scene understanding from single view 360 video. In *2018 International Conference on 3D Vision (3DV)*, pages 334–342. IEEE, 2018. 2
- [20] Oliver Glauser, Shihao Wu, Daniele Panozzo, Otmar Hilliges, and Olga Sorkine-Hornung. Interactive hand pose estimation using a stretch-sensing soft glove. *ACM Transactions on Graphics (TOG)*, 38(4):1–15, 2019. 1, 2
- [21] Helmut Grabner, Juergen Gall, and Luc Van Gool. What makes a chair a chair? In *CVPR 2011*, pages 1529–1536. IEEE, 2011. 2
- [22] Abhinav Gupta, Scott Satkin, Alexei A Efros, and Martial Hebert. From 3d scene geometry to human workspace. In *CVPR 2011*, pages 1961–1968. IEEE, 2011. 2
- [23] Vladimir Guzov, Aymen Mir, Torsten Sattler, and Gerard Pons-Moll. Human poseitioning system (hps): 3d human pose estimation and self-localization in large scenes from body-mounted sensors. In *Proceedings of the IEEE/CVF Conference on Computer Vision and Pattern Recognition*, pages 4318–4329, 2021. 2
- [24] Mohamed Hassan, Duygu Ceylan, Ruben Villegas, Jun Saito, Jimei Yang, Yi Zhou, and Michael J Black. Stochastic scene-aware motion prediction. In *Proceedings of the IEEE/CVF International Conference on Computer Vision*, pages 11374–11384, 2021. 2, 16, 22
- [25] Mohamed Hassan, Vasileios Choutas, Dimitrios Tzionas, and Michael J Black. Resolving 3d human pose ambiguities with 3d scene constraints. In *Proceedings of the IEEE/CVF International Conference on Computer Vision*, pages 2282–2292, 2019. 2
- [26] Mohamed Hassan, Partha Ghosh, Joachim Tesch, Dimitrios Tzionas, and Michael J Black. Populating 3d scenes

- by learning human-scene interaction. In *Proceedings of the IEEE/CVF Conference on Computer Vision and Pattern Recognition*, pages 14708–14718, 2021. 2
- [27] Ruizhen Hu, Oliver van Kaick, Bojian Wu, Hui Huang, Ariel Shamir, and Hao Zhang. Learning how objects function via co-analysis of interactions. *ACM Transactions on Graphics (TOG)*, 35(4):1–13, 2016. 2
- [28] Siyuan Huang, Siyuan Qi, Yixin Zhu, Yinxue Xiao, Yuanlu Xu, and Song-Chun Zhu. Holistic 3d scene parsing and reconstruction from a single rgb image. In *Proceedings of the European Conference on Computer Vision (ECCV)*, pages 187–203, 2018. 1
- [29] Yinghao Huang, Manuel Kaufmann, Emre Aksan, Michael J Black, Otmar Hilliges, and Gerard Pons-Moll. Deep inertial poser: Learning to reconstruct human pose from sparse inertial measurements in real time. *ACM Transactions on Graphics (TOG)*, 37(6):1–15, 2018. 1, 2
- [30] Yun Jiang, Hema Koppula, and Ashutosh Saxena. Hallucinated humans as the hidden context for labeling 3d scenes. In *Proceedings of the IEEE Conference on Computer Vision and Pattern Recognition*, pages 2993–3000, 2013. 2
- [31] Yun Jiang, Hema S Koppula, and Ashutosh Saxena. Modeling 3d environments through hidden human context. *IEEE transactions on pattern analysis and machine intelligence*, 38(10):2040–2053, 2015. 2
- [32] Yun Jiang, Marcus Lim, and Ashutosh Saxena. Learning object arrangements in 3d scenes using human context. *arXiv preprint arXiv:1206.6462*, 2012. 2
- [33] Mubbasir Kapadia, Xu Xianghao, Maurizio Nitti, Marcelo Kallmann, Stelian Coros, Robert W Sumner, and Markus Gross. Precision: Precomputing environment semantics for contact-rich character animation. In *Proceedings of the 20th ACM SIGGRAPH Symposium on Interactive 3D Graphics and Games*, pages 29–37, 2016. 2
- [34] Manuel Kaufmann, Yi Zhao, Chengcheng Tang, Lingling Tao, Christopher Twigg, Jie Song, Robert Wang, and Otmar Hilliges. Em-pose: 3d human pose estimation from sparse electromagnetic trackers. In *Proceedings of the IEEE/CVF International Conference on Computer Vision*, pages 11510–11520, 2021. 2
- [35] Vladimir G Kim, Siddhartha Chaudhuri, Leonidas Guibas, and Thomas Funkhouser. Shape2pose: Human-centric shape analysis. *ACM Transactions on Graphics (TOG)*, 33(4):1–12, 2014. 2
- [36] Weicheng Kuo, Anelia Angelova, Tsung-Yi Lin, and Angela Dai. Mask2cad: 3d shape prediction by learning to segment and retrieve. In *Computer Vision–ECCV 2020: 16th European Conference, Glasgow, UK, August 23–28, 2020, Proceedings, Part III 16*, pages 260–277. Springer, 2020. 1
- [37] Weicheng Kuo, Anelia Angelova, Tsung-Yi Lin, and Angela Dai. Patch2cad: Patchwise embedding learning for in-the-wild shape retrieval from a single image. In *Proceedings of the IEEE/CVF International Conference on Computer Vision*, pages 12589–12599, 2021. 1
- [38] Jehee Lee, Jinxiang Chai, Paul SA Reitsma, Jessica K Hodgins, and Nancy S Pollard. Interactive control of avatars animated with human motion data. In *Proceedings of the 29th annual conference on Computer graphics and interactive techniques*, pages 491–500, 2002. 2
- [39] Kang Hoon Lee, Myung Geol Choi, and Jehee Lee. Motion patches: building blocks for virtual environments annotated with motion data. In *ACM SIGGRAPH 2006 Papers*, pages 898–906. 2006. 2
- [40] Huajun Liu, Xiaolin Wei, Jinxiang Chai, Inwoo Ha, and Tae-hyun Rhee. Realtime human motion control with a small number of inertial sensors. In *Symposium on interactive 3D graphics and games*, pages 133–140, 2011. 2
- [41] Wei Mao, Miaomiao Liu, and Mathieu Salzmann. History repeats itself: Human motion prediction via motion attention. In *European Conference on Computer Vision*, pages 474–489. Springer, 2020. 5, 6, 13, 14
- [42] Josh Merel, Saran Tunyasuvunakool, Arun Ahuja, Yuval Tassa, Leonard Hasenclever, Vu Pham, Tom Erez, Greg Wayne, and Nicolas Heess. Catch & carry: reusable neural controllers for vision-guided whole-body tasks. *ACM Transactions on Graphics (TOG)*, 39(4):39–1, 2020. 2
- [43] Aron Monszpart, Paul Guerrero, Duygu Ceylan, Ersin Yumer, and Niloy J Mitra. imapper: interaction-guided scene mapping from monocular videos. *ACM Transactions On Graphics (TOG)*, 38(4):1–15, 2019. 2
- [44] Raul Mur-Artal, Jose Maria Martinez Montiel, and Juan D Tardos. Orb-slam: a versatile and accurate monocular slam system. *IEEE transactions on robotics*, 31(5):1147–1163, 2015. 1
- [45] Claudio Mura, Renato Pajarola, Konrad Schindler, and Niloy Mitra. Walk2map: Extracting floor plans from indoor walk trajectories. In *Computer Graphics Forum*, volume 40, pages 375–388. Wiley Online Library, 2021. 2
- [46] Richard A Newcombe, Shahram Izadi, Otmar Hilliges, David Molyneaux, David Kim, Andrew J Davison, Pushmeet Kohi, Jamie Shotton, Steve Hodges, and Andrew Fitzgibbon. Kinectfusion: Real-time dense surface mapping and tracking. In *2011 10th IEEE international symposium on mixed and augmented reality*, pages 127–136. IEEE, 2011. 1
- [47] Yinyu Nie, Xiaoguang Han, Shihui Guo, Yujian Zheng, Jian Chang, and Jian Jun Zhang. Total3dunderstanding: Joint layout, object pose and mesh reconstruction for indoor scenes from a single image. In *IEEE/CVF Conference on Computer Vision and Pattern Recognition (CVPR)*, June 2020. 1
- [48] Yinyu Nie, Ji Hou, Xiaoguang Han, and Matthias Nießner. Rfd-net: Point scene understanding by semantic instance reconstruction. In *Proceedings of the IEEE/CVF Conference on Computer Vision and Pattern Recognition*, pages 4608–4618, 2021. 14
- [49] Matthias Nießner, Michael Zollhöfer, Shahram Izadi, and Marc Stamminger. Real-time 3d reconstruction at scale using voxel hashing. *ACM Transactions on Graphics (ToG)*, 32(6):1–11, 2013. 1
- [50] Alessandro Pieropan, Carl Henrik Ek, and Hedvig Kjellström. Functional object descriptors for human activity modeling. In *2013 IEEE International Conference on Robotics and Automation*, pages 1282–1289. IEEE, 2013. 2
- [51] Stefan Popov, Pablo Bauszat, and Vittorio Ferrari. Corenet: Coherent 3d scene reconstruction from a single rgb image. In

- European Conference on Computer Vision*, pages 366–383. Springer, 2020. 1
- [52] Xavier Puig, Kevin Ra, Marko Boben, Jiaman Li, Tingwu Wang, Sanja Fidler, and Antonio Torralba. Virtualhome: Simulating household activities via programs. In *Proceedings of the IEEE Conference on Computer Vision and Pattern Recognition*, pages 8494–8502, 2018. 5, 12, 14
- [53] Charles R. Qi, Or Litany, Kaiming He, and Leonidas J. Guibas. Deep hough voting for 3d object detection in point clouds. In *Proceedings of the IEEE/CVF International Conference on Computer Vision (ICCV)*, October 2019. 4, 5, 6, 13, 14
- [54] Shengyi Qian, Linyi Jin, and David F Fouhey. Associative3d: Volumetric reconstruction from sparse views. In *European Conference on Computer Vision*, pages 140–157. Springer, 2020. 1
- [55] Eduardo Ruiz and Walterio Mayol-Cuevas. Where can i do this? geometric affordances from a single example with the interaction tensor. In *2018 IEEE International Conference on Robotics and Automation (ICRA)*, pages 2192–2199. IEEE, 2018. 2
- [56] Martin Runz, Kejie Li, Meng Tang, Lingni Ma, Chen Kong, Tanner Schmidt, Ian Reid, Lourdes Agapito, Julian Straub, Steven Lovegrove, et al. Frodo: From detections to 3d objects. In *Proceedings of the IEEE/CVF Conference on Computer Vision and Pattern Recognition*, pages 14720–14729, 2020. 1
- [57] Manolis Savva, Angel X Chang, Pat Hanrahan, Matthew Fisher, and Matthias Nießner. Scenegrok: Inferring action maps in 3d environments. *ACM transactions on graphics (TOG)*, 33(6):1–10, 2014. 2
- [58] Manolis Savva, Angel X Chang, Pat Hanrahan, Matthew Fisher, and Matthias Nießner. Pigraphs: learning interaction snapshots from observations. *ACM Transactions on Graphics (TOG)*, 35(4):1–12, 2016. 2
- [59] Johann Sawatzky, Abhilash Srikantha, and Juergen Gall. Weakly supervised affordance detection. In *Proceedings of the IEEE Conference on Computer Vision and Pattern Recognition*, pages 2795–2804, 2017. 2
- [60] Muhammad Shoaib, Michael Ying Yang, Bodo Rosenhahn, and Joern Ostermann. Estimating layout of cluttered indoor scenes using trajectory-based priors. *Image and Vision Computing*, 32(11):870–883, 2014. 2
- [61] Hubert PH Shum, Taku Komura, Masashi Shiraishi, and Shuntaro Yamazaki. Interaction patches for multi-character animation. *ACM Transactions on Graphics (TOG)*, 27(5):1–8, 2008. 2
- [62] Sebastian Starke, He Zhang, Taku Komura, and Jun Saito. Neural state machine for character-scene interactions. *ACM Trans. Graph.*, 38(6):209–1, 2019. 2
- [63] Timo Von Marcard, Bodo Rosenhahn, Michael J Black, and Gerard Pons-Moll. Sparse inertial poser: Automatic 3d human pose estimation from sparse imus. In *Computer Graphics Forum*, volume 36, pages 349–360. Wiley Online Library, 2017. 1, 2
- [64] Jiashun Wang, Huazhe Xu, Jingwei Xu, Sifei Liu, and Xiaolong Wang. Synthesizing long-term 3d human motion and interaction in 3d scenes. In *Proceedings of the IEEE/CVF Conference on Computer Vision and Pattern Recognition*, pages 9401–9411, 2021. 2
- [65] Zhe Wang, Liyan Chen, Shaurya Rathore, Daeyun Shin, and Charles Fowlkes. Geometric pose affordance: 3d human pose with scene constraints. *arXiv preprint arXiv:1905.07718*, 2019. 2
- [66] Ping Wei, Yibiao Zhao, Nanning Zheng, and Song-Chun Zhu. Modeling 4d human-object interactions for joint event segmentation, recognition, and object localization. *IEEE transactions on pattern analysis and machine intelligence*, 39(6):1165–1179, 2016. 2
- [67] Thomas Whelan, Stefan Leutenegger, R Salas-Moreno, Ben Glocker, and Andrew Davison. Elasticfusion: Dense slam without a pose graph. Robotics: Science and Systems, 2015. 1
- [68] Jiajun Wu, Chengkai Zhang, Tianfan Xue, William T Freeman, and Joshua B Tenenbaum. Learning a probabilistic latent space of object shapes via 3d generative-adversarial modeling. In *Proceedings of the 30th International Conference on Neural Information Processing Systems*, pages 82–90, 2016. 6, 14
- [69] Rundi Wu, Xuelin Chen, Yixin Zhuang, and Baoquan Chen. Multimodal shape completion via conditional generative adversarial networks. In *Computer Vision–ECCV 2020: 16th European Conference, Glasgow, UK, August 23–28, 2020, Proceedings, Part IV 16*, pages 281–296. Springer, 2020. 5, 14
- [70] Sijie Yan, Yuanjun Xiong, and Dahua Lin. Spatial temporal graph convolutional networks for skeleton-based action recognition. In *Thirty-second AAAI conference on artificial intelligence*, 2018. 3, 12
- [71] Tianwei Yin, Xingyi Zhou, and Philipp Krahenbuhl. Center-based 3d object detection and tracking. In *Proceedings of the IEEE/CVF Conference on Computer Vision and Pattern Recognition*, pages 11784–11793, 2021. 4
- [72] Cheng Zhang, Zhaopeng Cui, Yinda Zhang, Bing Zeng, Marc Pollefeys, and Shuaicheng Liu. Holistic 3d scene understanding from a single image with implicit representation. In *Proceedings of the IEEE/CVF Conference on Computer Vision and Pattern Recognition (CVPR)*, pages 8833–8842, June 2021. 1
- [73] Siwei Zhang, Yan Zhang, Qianli Ma, Michael J Black, and Siyu Tang. Place: Proximity learning of articulation and contact in 3d environments. In *2020 International Conference on 3D Vision (3DV)*, pages 642–651. IEEE, 2020. 2
- [74] Yan Zhang, Mohamed Hassan, Heiko Neumann, Michael J Black, and Siyu Tang. Generating 3d people in scenes without people. In *Proceedings of the IEEE/CVF Conference on Computer Vision and Pattern Recognition*, pages 6194–6204, 2020. 2
- [75] Yixin Zhu, Yibiao Zhao, and Song Chun Zhu. Understanding tools: Task-oriented object modeling, learning and recognition. In *Proceedings of the IEEE Conference on Computer Vision and Pattern Recognition*, pages 2855–2864, 2015. 2

Appendix

In the supplementary material, we describe network parameters and specifications (Sec. A), details of our data generation and distribution (Sec. B), evaluation metrics in our experiments (Sec. C), additional quantitative results (Sec. D), additional qualitative results (Sec. E), and qualitative results on real data (Sec F).

A. Network Specifications

We detail the full list of network parameters and specifications in this section. MLP layers used in our network are uniformly denoted by $\text{MLP}[l_1, l_2, \dots, l_d]$, where l_i is the neuron number in the i -th layer. Each layer is followed by a batch normalization and a ReLU layer except the final one. We also report the efficiency and memory usage during inference at the end. Our code will be publicly available.

A.1. Skeleton Configuration

In P2R-Net, the input is a pose trajectory with N frames and J joints as the sequence of 3D locations $T \in \mathbb{R}^{N \times J \times 3}$, where $N = 768$, $J = 53$. For each trajectory, the humanoid agent interacts with up to 10 different objects in a scene, with the frame number varying among sequences (depending on the object interactions). To enable mini-batch training, we uniformly sample N frames per sequence for training.

For the human skeleton structure, we use the predefined human body model in VirtualHome [52], which uses the Unity3D human body template. We refer readers to [1] for the detailed definition of the skeleton specifications. The root joint $r \in \mathbb{R}^{N \times 3}$ that we use is the centroid of the hips, as illustrated in Figure 9.

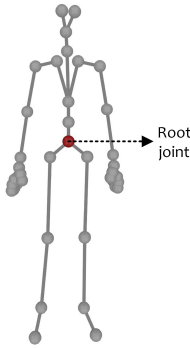


Figure 9. Human skeleton configuration, following VirtualHome [52].

A.2. Relative Position Encoder

We list the layer details of our relative position encoder in Figure 10. In Section 3.1, the output pose feature dimension $d_1 = 64$, the number of temporal neighbors $k = 20$.

From the input pose trajectory T , it outputs the relative pose features $P^r \in \mathbb{R}^{N \times J \times 64}$ for spatio-temporal encoding.

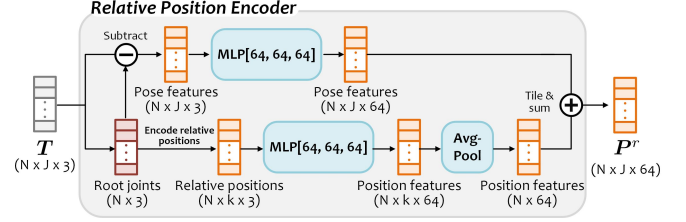


Figure 10. Relative position encoder.

A.3. Spatio-Temporal Pose Encoder

Figure 11 illustrates the layer details of our spatio-temporal pose encoder in Section 3.2. From the input pose feature P^r , we use a graph convolutional layer to learn intra-skeleton joint features. Edges in the graph convolution are constructed following the skeleton bones (as in Figure 9), which encodes skeleton-wise spatial information. We use the method of [70] to build the edge connections from skeleton bones. With the learned joint features on each skeleton, we then adopt a 1-D convolutional layer (feature dimension at 64, kernel size at 3, padding size at 1) to process joint features in temporal domain. The kernel size presents its receptive field on neighboring frames. We connect a graph layer and a 1-D convolutional layer into a block with a residual summation from the input (see Figure 11). We duplicate the block six times and stack them in a sequence to construct the spatio-temporal pose encoder. After the spatio-temporal layers, we then flatten all joint features in a skeleton, which results in a $64J$ -dimensional feature per pose, followed by an $\text{MLP}[256]$ to process each pose and produce the final spatio-temporal pose features $P^{st} \in \mathbb{R}^{N \times d_2}$. $d_2 = 256$.

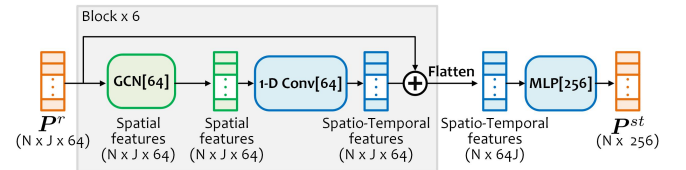


Figure 11. Spatio-temporal pose encoder.

A.4. Locality-Sensitive Voting

In Section 3.3 of the main paper, we sample M seeds r_s from root joints r , where $M = 512$. The M seeds are uniformly sampled along the trajectory of root joints to ensure a even spatial distribution. P_s^{st} are the corresponding pose features of r_s , where $r_s \in \mathbb{R}^{M \times 3}$, $P_s^{st} \in \mathbb{R}^{M \times d_2}$, $d_2 = 256$. In Eq. 2 of the paper, we use two MLPs, f_3 and

f_4 , to learn the vote locations and features (v, P^v) from (r_s, P_s^{st}) , where f_3 and f_4 share the first two MLP layers and correspondingly predict their targets from the last layer. We illustrate them in Figure 12.

From the 512 votes (v, P^v) , we group them into V clusters following [53], which results in (v^c, P^c) cluster centers and features, where $v^c \in \mathbb{R}^{V \times 3}$, $P^c \in \mathbb{R}^{V \times 256}$, $V=128$. For poses whose root joint is not close to any object during training (beyond a distance threshold $t_d=1$ m), we do not consider them to vote for any object.

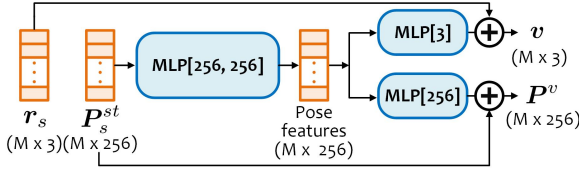


Figure 12. Locality-sensitive voting.

A.5. Probabilistic Mixture Decoder

In Section 3.4 of the main paper, we learn multiple Gaussian distributions $\mathcal{N}(\mu_\tau^k, \Sigma_\tau^k)$ for each regression target $\tau \in \{c, s, \theta\}$, $k=1, \dots, P$, where c, s, θ respectively denote the box center, size and orientation; P is the number of distributions ($P=100$). For each distribution, we also learn a mode score $f_\tau^k(*) \in [0, 1]$ as its weight in predicting the target (see Eq.3 in the paper). $v^c \in v^c$, $P^c \in P^c$ represent a cluster center and feature, from which a proposal box is predicted.

The learnable parameters are $\{(\mu_\tau, \Sigma_\tau)\}$ and $\{f_\tau\}$, where $\mu_\tau \in \mathbb{R}^{P \times d_\tau}$; $\Sigma_\tau \in \mathbb{R}^{P \times d_\tau \times d_\tau}$. For each target $\tau \in \{c, s, \theta\}$, μ_τ represents the mean values of the P Gaussian distributions, and Σ_τ stores the corresponding covariance matrices. $\mu_\tau^k \in \mathbb{R}^{d_\tau}$ and $\Sigma_\tau^k \in \mathbb{R}^{d_\tau \times d_\tau}$ are the k -th item in μ_τ and Σ_τ respectively. d_τ is the dimension for each target, where $d_c=3$; $d_s=3$; $d_\theta=2$. Here we consider variables in each Gaussian are independently distributed, resulting in a diagonal covariance matrix. We formulate $\{(\mu_\tau, \Sigma_\tau)\}$ as learnable embeddings shared among all samples in training and testing. Since covariance matrix in Σ_τ is diagonal and non-negative, we use an exponential function to process its diagonal elements.

f_τ is realized with an MLP layer to predict mode scores for each target, where we use MLP[128,128,128,100] appended with a sigmoid layer.

For the proposal objectness and probability distribution of class category, we predict them directly from P^c with MLP[128,128, $d_{obj}+d_{cls}$], where $d_{obj}=2$ and $d_{cls}=17$ (the number of object categories), followed by a softmax layer to get their probability scores in $[0, 1]$.

To generate a hypothesis for each object during inference, we sample box parameters with Eq. 4 in our paper.

Each hypothesis is an average of N_s samples of y_τ . N_s is also a random number in $[1, 100]$. Additionally, we sample the object class based on the predicted classification probability distribution.

We discard proposed object boxes which have low objectness scores ($\leq t_o$) after a 3D non-maximum suppression ($t_o = 0.5$), which then outputs N_h hypotheses in a scene.

A.6. Efficiency and Memory in Inference

We train our network with batch size of 32 with 4 NVIDIA RTX 2080 GPUs using PyTorch 1.7.1, and test it with a single GPU. We report the model size, inference timing and allocated GPU memory in a single forward pass.

Model size	Avg. time	Peak. time	Avg. memory	Peak memory
2.04 M	0.092 s	0.582 s	11.64 MB	260.82 MB

Table 6. Model size, efficiency and memory usage of P2R-Net.

A.7. Specifications of Baselines

We explain the network details of each baseline as the following.

Pose-VoteNet Pose-VoteNet is a variant of VoteNet [53] to make it able to vote for object centers from human poses. In our experiments, we replace the PointNet++ in original VoteNet with our position encoder, which produces relative pose feature $P^r \in \mathbb{R}^{N \times J \times 64}$. We then flatten all joint features for each pose ($\mathbb{R}^{N \times 64 \times J}$) and learn the seed feature with MLP[256, 256, 256]. The coordinates of each seed is located at the root joint, similar with ours. For the remaining structures and loss functions, we keep them consistent with VoteNet.

Pose-VN To make Pose-VoteNet able to capture rotation information of poses, we augment it by replacing MLP layers in Pose-VoteNet encoder with vector neurons [12]. Vector neurons are a set of SO(3)-equivariant operators that capture arbitrary rotations of object poses to estimate objects. For each MLP layer in Pose-VoteNet encoder, we replace it with a ‘VNLinearLeakyReLU’ layer, and the final MLP layer with a ‘VNLinear’ layer, with equal number of parameters. For the details of layer design in vector neurons, we refer readers to [12].

Motion Attention We replace the MLP layers (i.e., MLP[256, 256, 256]) in Pose-VoteNet encoder with the attention module in [41] to learn inter-frame pose features in the entire temporal domain. Specifically, for each pose feature in P^r , we use it to query similar features among all frames, which assembles repetitive pose patterns to regress

object boxes. For the layer details in motion attention, we refer readers to [41].

P2R-Net-D We replace our probabilistic decoder with the VoteNet decoder [53] along with their loss functions to produce deterministic results.

P2R-Net-G We ablate the P2R-Net decoder with a probabilistic generative model [48, 68], where we first learn a latent code $z \sim \mathcal{N}(\mathbf{0}, \mathbf{1})$ from cluster features P^c . By decoding from the summation of z and $P^c \in P^c$, we can predict box parameters in a probabilistic generative way.

P2R-Net-H We discretize each regression target into a binary heatmap, where box centers are discretized into 10^3 bins in $[-0.3 \text{ m}, 0.3 \text{ m}]^3$, centered at cluster centers v^c ; box sizes are discretized into 10^3 bins in $[0.05 \text{ m}, 3 \text{ m}]^3$; box orientations are discretized into 12 bins in $[-\pi, \pi]$. Then the box regression is converted into a classification task. We train them by cross-entropy losses. In testing, we sample the heatmaps to produce different predictions.

B. Data Generation and Data Statistics

We create our dataset using the VirtualHome simulation environment [52], which is built on the Unity3D game engine. It consists of 29 rooms, where each room has 88 objects on average. Each object is annotated with available interaction types. For the detailed specification of interaction manners for different object categories, we refer to [2, 52].

VirtualHome allows users to customize action scripts to direct humanoid agents to execute a series of complex interactive tasks. In our work, we focus on the static, interactable objects under 17 common class categories (i.e., bed, bench, bookshelf, cabinet, chair, desk, dishwasher, faucet, fridge, lamp, microwave, monitor, nightstand, sofa, stove, toilet, computer).

In each room, we select up to 10 random objects in the scene, and script the agent to interact with each of the objects in a sequential fashion. For each object, we also select a random interaction type associated with the object class category. Sequences are trained with and evaluated against only the objects that are interacted with during the input observation, resulting in different variants of each room under different interaction sequences.

Then we randomly sample 13,913 different sequences with corresponding object boxes to construct the dataset. The human pose trajectories are recorded with a frame rate of 5 frames per second. Over the sequences, the average number of objects is 7.86, and the average frame length is 509.34. The distributions of the frame length and object number in a interaction trajectory are shown in Figure 14 and Figure 13. The interaction frequency for each object

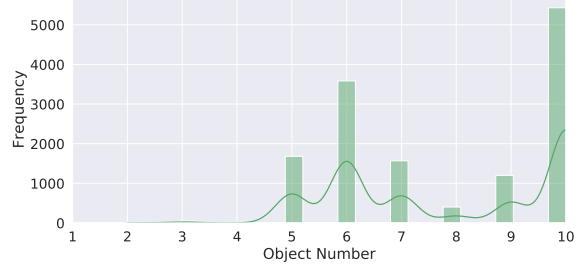


Figure 13. Distribution over number of objects in a pose trajectory.

class category is illustrated in Figure 15, and we also list the frequency of each interaction type in Figure 16.

C. Evaluation Metrics

In our method, we use mAP@0.5 to evaluate the detection accuracy by comparing our maximum likelihood prediction with the ground-truth. We also use Minimal Matching Distance (MMD) and Total Mutual Diversity (TMD) to respectively evaluate the quality and diversity of our multi-modal predictions. For each input sequence, we sample our probabilistic mixture decoder and produce 10 hypotheses of object arrangements. We adapt MMD from [3] to evaluate our task, and measure the best matching mAP@0.5 score with the ground-truth out of the 10 hypotheses. For TMD, we follow [69] to evaluate the multi-modality of our predictions, formulated as

$$\begin{aligned}
 \text{TMD}(O^i) &= [1 + \text{Entropy}(\mathcal{C}(O^i))] \cdot [1 + \text{Div}(\mathcal{B}(O^i))], \\
 \text{Div}(\mathcal{B}(O^i)) &= \frac{1}{10} \sum_{p=1}^{10} \sum_{q=1}^{10} \text{Dist}(B_p^i, B_q^i), \\
 \text{Dist}(B_p^i, B_q^i) &= \frac{1}{8} \sum_{j=1}^8 \|P - Q\|_2, \quad P \in B_p^i, Q \in B_q^i, \\
 \mathcal{C}(O^i) &= \{c_1^i, c_2^i, \dots, c_{10}^i\}, \\
 \mathcal{B}(O^i) &= \{B_1^i, B_2^i, \dots, B_{10}^i\}, \quad B_k^i \in \mathbb{R}^{8 \times 3}.
 \end{aligned} \tag{5}$$

In Eq. 5, TMD is defined at the object-level; for each object O^i in a scene, we have 10 hypotheses which are represented by 10 bounding boxes $\mathcal{B}(O^i)$ with the corresponding 10 predicted class labels $\mathcal{C}(O^i)$; B_k^i is the k -th hypothesis in $\mathcal{B}(O^i)$, which can be represented by a point set with eight box corners, and c_k^i is the corresponding class label; $\text{Entropy}(\cdot)$ denotes the Shannon Entropy to measure the variance of class labels; $\text{Div}(\cdot)$ measures the diversity of predicted bounding boxes among hypotheses, which is defined by the average of distance sum from a hypothesis B_p^i to all other hypotheses; $\text{Dist}(\cdot)$ is the average Euclidean distance between pair-wise points from B_p^i and B_q^i .

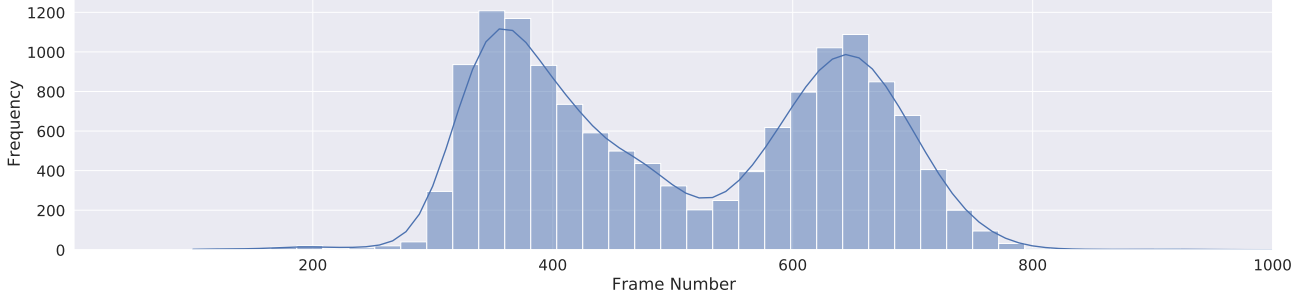


Figure 14. Distribution of frame lengths in pose trajectories.

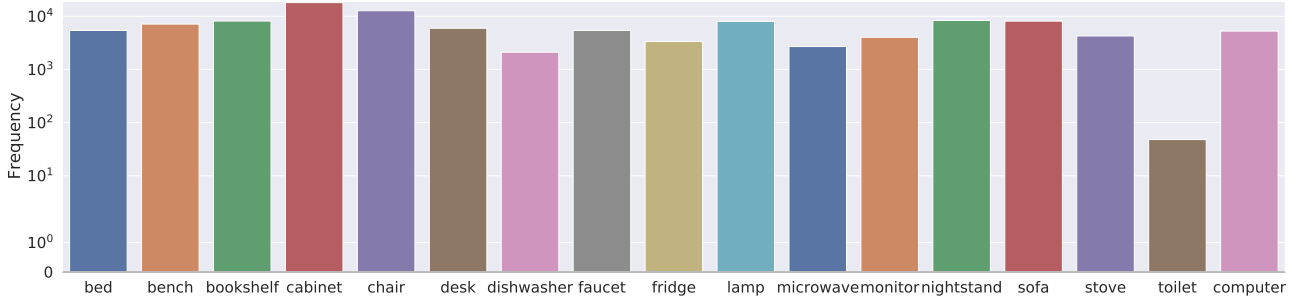


Figure 15. Frequency of object class categories among generated interactions.

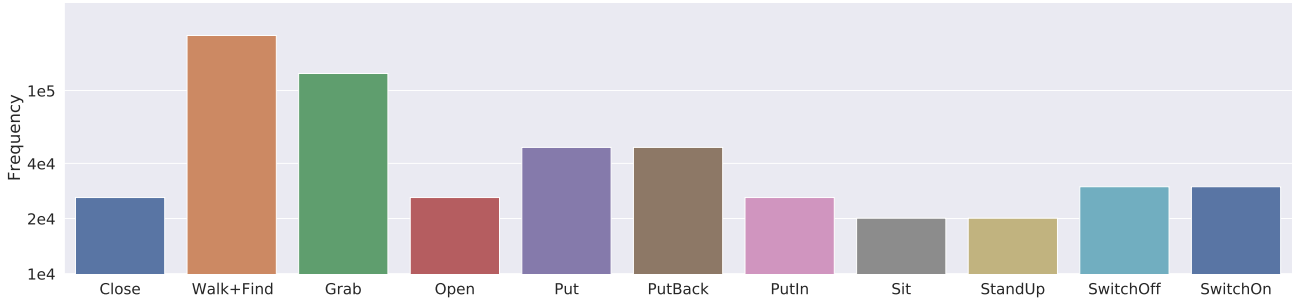


Figure 16. Frequency of interaction types.

$TMD(O^i)=1$ if all hypotheses are the same, where $\mathcal{C}(O^i)=0$; $Div(\mathcal{B}(O^i)) = 0$, which indicates no diversity. In Section 5.3 of the main paper, we report the average TMD score over all objects.

D. Additional Quantitative Results

We list the mAP@0.5 scores on all object categories by split \mathcal{S}_1 and \mathcal{S}_2 in Table 7 and Table 8 respectively. P2R-Net variants are evaluated by the maximum likelihood predictions to calculate mAP scores. Note that there are fewer categories in the test set of \mathcal{S}_2 .

E. Additional Qualitative Results

We show additional qualitative results on test splits \mathcal{S}_1 and \mathcal{S}_2 in Figures 17-19 and 20, respectively. We additionally visualize various multi-modal predictions from our model on \mathcal{S}_1 in Figure 21.

F. Qualitative Results on Real Data

To the best of our knowledge, there are no real datasets labeled with multi-object scenes and various human-scene interaction trajectories for our training. To explore our generalization ability in real data, we qualitatively evaluate P2R-Net by training it on our dataset, and apply it to the

	bed	bench	bkshlf	cabnt	chair	desk	dishws	faucet	fridge	lamp	microw	monitor	nstand	sofa	stove	toilet	cmpter	mAP@0.5
Pose-VoteNet	2.90	15.00	73.79	33.14	18.77	58.52	32.14	0.00	0.00	6.07	6.49	23.55	51.30	62.32	49.82	0.00	3.06	25.70
Pose-VoteNet + VN	20.81	18.13	78.25	49.76	18.68	70.92	33.56	0.00	0.00	5.60	5.23	22.71	64.46	67.24	46.76	0.00	6.11	29.90
Motion Attention	36.42	7.54	66.25	23.35	19.50	77.71	15.59	0.03	17.13	2.35	6.42	29.87	30.59	78.61	51.03	14.81	5.50	28.39
P2R-Net-D	93.77	12.63	37.21	11.98	5.77	95.93	61.80	0.10	73.95	0.58	7.39	9.68	9.62	88.44	70.42	0.00	14.17	34.91
P2R-Net-G	91.69	7.56	41.27	36.61	10.05	93.47	67.53	0.10	77.45	1.21	6.36	10.51	11.32	92.97	64.86	5.56	18.67	37.48
P2R-Net-H	85.84	8.04	43.78	22.04	10.91	76.08	55.20	0.00	55.15	0.00	1.57	4.24	20.31	83.92	57.60	5.00	4.33	31.41
Ours	94.21	10.12	41.75	54.72	8.02	93.32	56.33	0.06	59.89	3.25	6.49	12.84	46.53	90.92	57.86	61.11	19.94	42.20

Table 7. Quantitative evaluation on split \mathcal{S}_1 .

	bed	bench	bookshelf	cabinet	chair	desk	dishwasher	faucet	fridge	microwave	nightstand	stove	mAP@0.5
Pose-VoteNet	0.00	4.48	22.84	2.30	0.56	4.05	14.64	0.00	0.00	0.61	0.00	73.33	10.23
Pose-VN	0.00	0.96	19.88	7.99	0.51	0.14	10.61	0.00	0.00	0.00	0.01	33.33	6.12
Motion Attention	28.16	1.81	24.19	1.43	0.00	0.00	0.00	0.00	0.00	0.00	22.77	0.00	6.53
P2R-Net-D	39.86	25.17	26.78	3.29	0.18	56.53	76.39	0.00	86.50	30.75	0.00	33.33	31.56
P2R-Net-G	50.65	17.89	13.86	0.54	0.04	56.97	87.61	0.06	70.91	13.76	0.00	66.67	31.59
P2R-Net-H	48.22	10.43	39.12	15.12	0.02	41.26	71.18	0.00	76.10	0.69	0.01	33.33	27.96
P2R-Net	81.48	12.05	17.18	6.43	0.10	72.07	100.00	0.11	63.39	4.61	0.04	66.66	35.34

Table 8. Quantitative evaluation on split \mathcal{S}_2 .

real-world human pose trajectory data provided by [24] describing human interactions with single objects. The qualitative results are illustrated in Figure 22, where we see that our method still can provide plausible object explanations from natural and diverse real human poses.

bed bench bookshelf cabinet chair desk dishwasher faucet fridge lamp microwave monitor nightstand sofa stove toilet computer

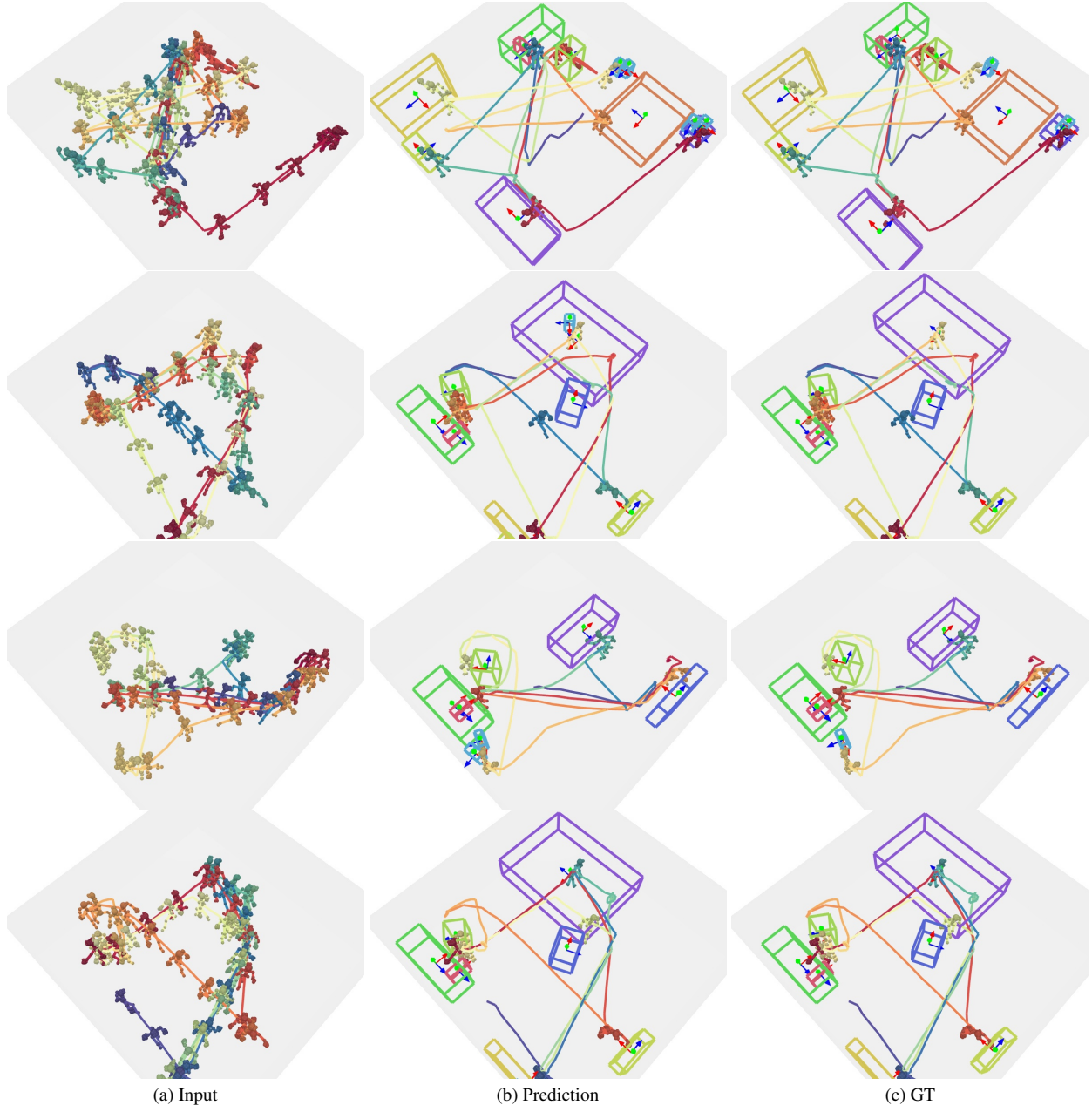


Figure 17. Additional results on estimating object layouts from a pose trajectory on the sequence-level split S_1 (unseen interaction sequences).

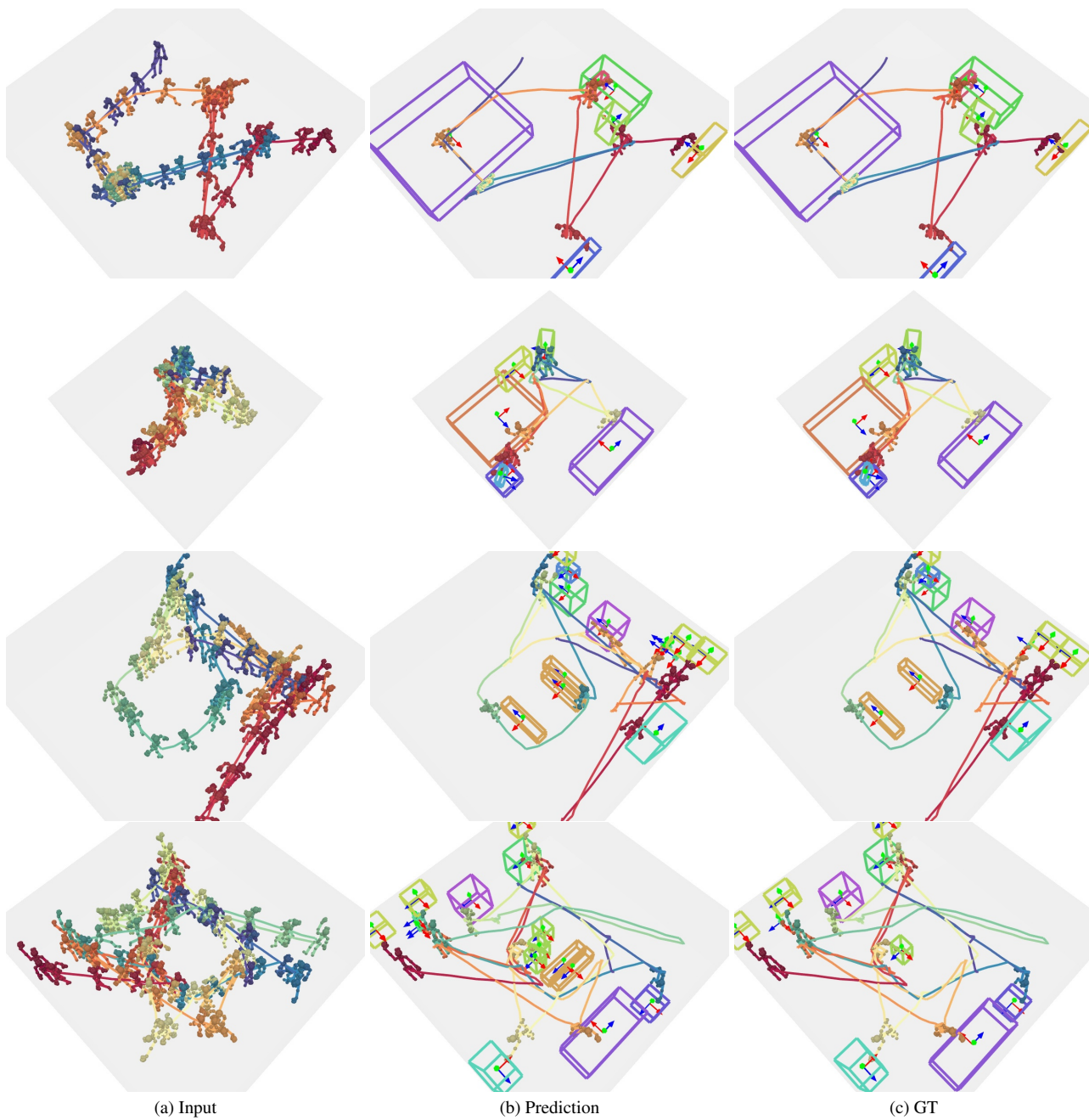


Figure 18. Additional results on estimating object layouts from a pose trajectory on the sequence-level split \mathcal{S}_1 (unseen interaction sequences).

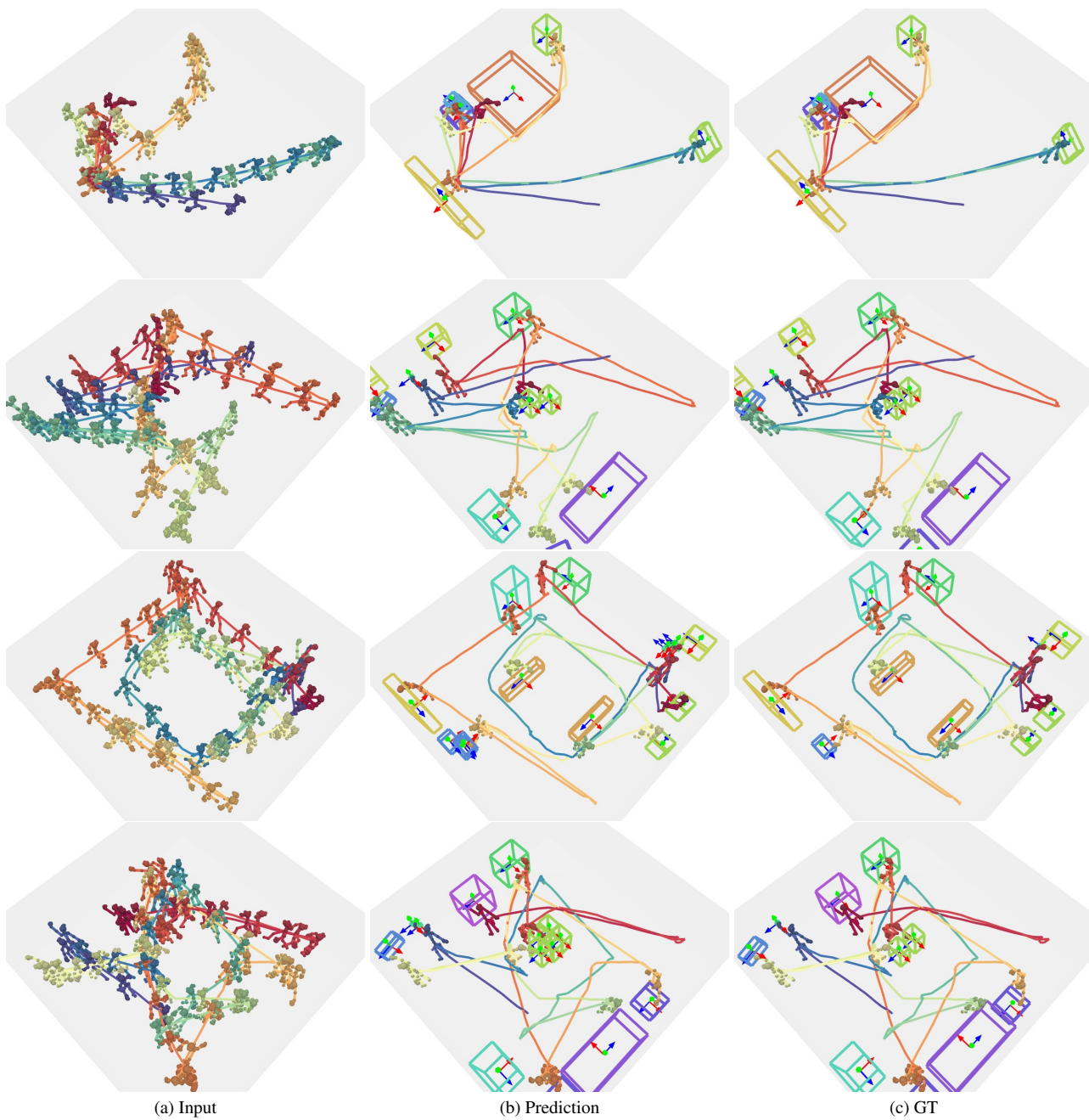


Figure 19. Additional results on estimating object layouts from a pose trajectory on the sequence-level split \mathcal{S}_1 (unseen interaction sequences).



Figure 20. Additional results on estimating object layouts from a pose trajectory on the room-level split S_2 (unseen interaction sequences and rooms).

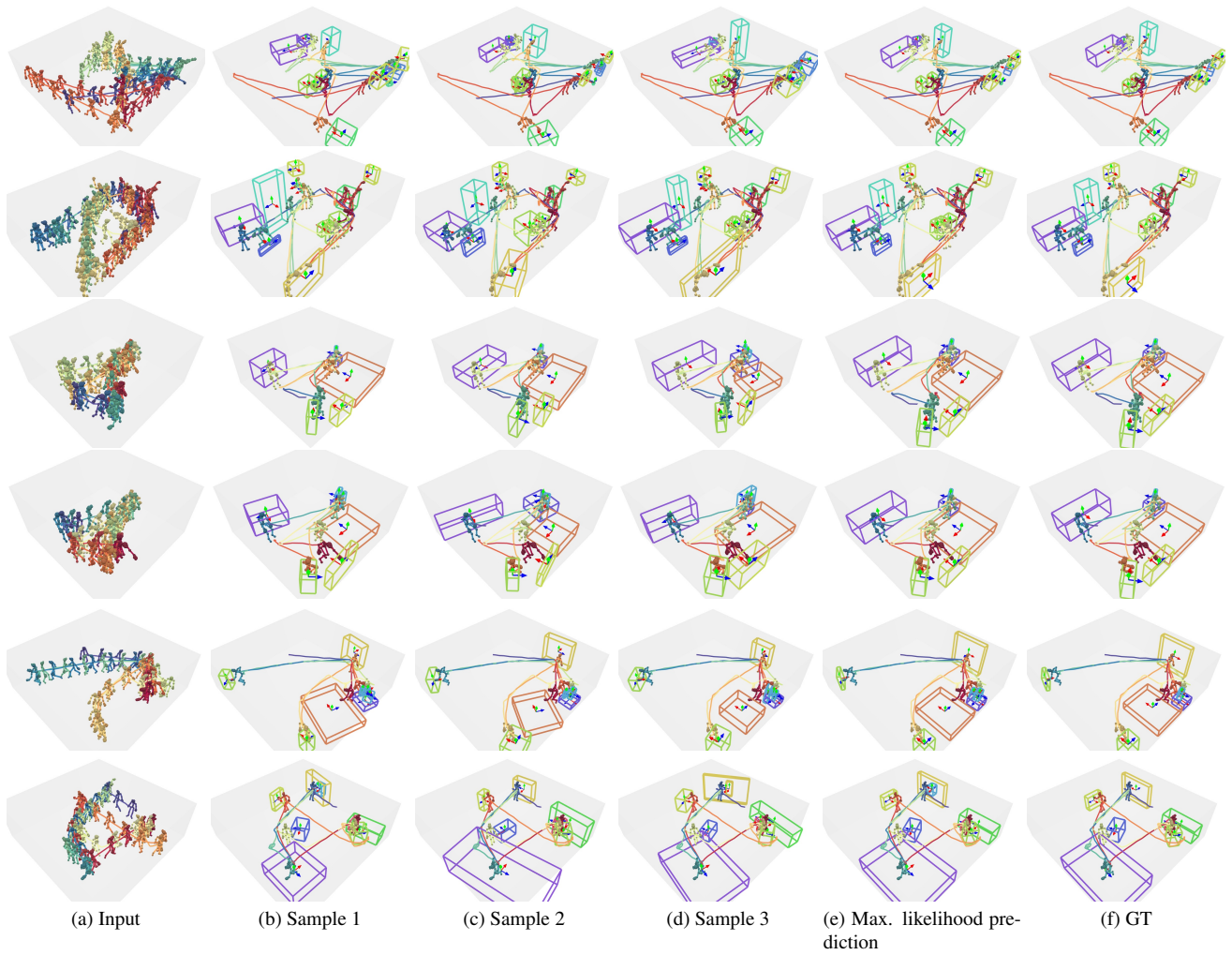


Figure 21. Additional multi-modal predictions of P2R-Net. By sampling our probabilistic decoder multiple times, we can obtain various different plausible box predictions.

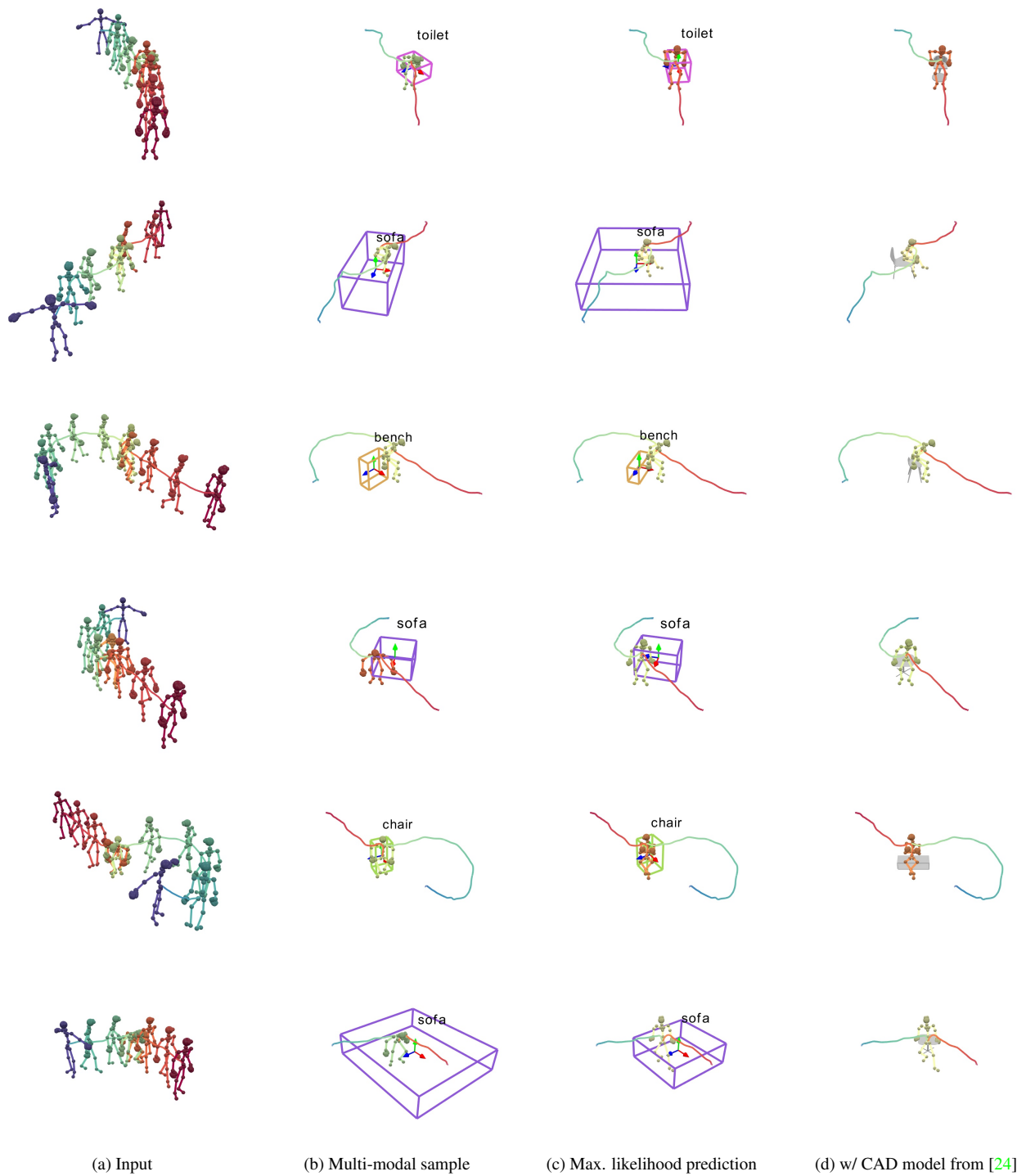


Figure 22. Multi-modal predictions on the real human pose trajectory input of [24].